


Dynamical Sweet Spot Engineering via Two-Tone Flux Modulation of Superconducting Qubits

Joseph A. Valery^{1,*}, Shoumik Chowdhury^{1,2}, Glenn Jones¹ and Nicolas Didier¹

¹*Rigetti Computing, 775 Heinz Avenue, Berkeley, California 94710, USA*

²*Department of Physics, Yale University, New Haven, Connecticut 06520, USA*

 (Received 30 June 2021; revised 28 February 2022; accepted 20 April 2022; published 18 May 2022)

Current superconducting quantum processors require strategies for coping with material defects and imperfect parameter targeting in order to scale up while maintaining high performance. To that end, *in situ* control of qubit frequencies with magnetic flux can be used to avoid spurious resonances. However, increased dephasing due to $1/f$ flux noise limits performance at all of these operating points except for noise-protected sweet spots, which are sparse under dc flux bias and monochromatic flux modulation. Here we experimentally demonstrate that two-tone flux modulation can be used to create a continuum of dynamical sweet spots, greatly expanding the range of qubit frequencies achievable while first-order insensitive to slow flux noise. To illustrate some advantages of this flexibility, we use bichromatic flux control to reduce the error rates and gate times of parametric entangling operations between transmons. Independent of the gate scheme, the ability to use flux control to freely select qubit frequencies while maintaining qubit coherence represents an important step forward in the robustness and scalability of near-term superconducting qubit devices.

DOI: [10.1103/PRXQuantum.3.020337](https://doi.org/10.1103/PRXQuantum.3.020337)

I. INTRODUCTION

As they scale, superconducting quantum computing architectures need the capability to contend with experimental imperfections. Two-level system (TLS) defects [1–7] and flawed frequency targeting due to variance in Josephson junction fabrication [8–18] are common sources of error for today’s processors. Taking advantage of modular device compositions [19–22] can help avoid these problems, but it is also necessary to use *in situ* control to cope with them as they arise. For example, the use of parallel Josephson junctions in a superconducting quantum interference device (SQUID) loop allows for the tunability of qubit frequency with magnetic flux, providing a convenient way to correct for variations from frequency targets as well as dodge coupled material defects. Additional pathways for control necessarily open up additional pathways for noise, however, and the cost of flux tunability is exposure to $1/f$ flux noise, which dephases tunable qubits [23–40]. Thus, it is important to develop control

schemes that minimize the time a qubit spends at sensitive operating points during a program in order to extend dephasing times [25,41–45].

Under a dc flux bias Φ_{dc} and a single-tone flux modulation with amplitude Φ_{ac} , flux-insensitive “sweet spot” operating points are sparse. There are six within a single flux period Φ_0 , corresponding to $\Phi_{dc} = 0, 0.5\Phi_0$ along with $\Phi_{ac} \approx 0, 0.6\Phi_0$, as well as $\Phi_{dc} = \pm 0.25\Phi_0$ along with $\Phi_{ac} \approx 0.4\Phi_0$ [46]. The result is only six time-averaged qubit frequencies \bar{f} that are achievable without exposing the qubit to flux noise-induced dephasing. However, a recent theory proposal suggests that the introduction of a second flux modulation tone can provide a pathway to achieving more flexibility [47]. Whereas a dc flux bias provides two sweet spots per flux period and a single tone of modulation introduces four more, bichromatic modulation unlocks a continuum of operating points that are first-order insensitive to $1/f$ flux noise. Control of the frequency relationship, mixing, and relative phase of the two tones can significantly shift a tunable qubit’s average frequency under modulation, creating dynamical sweet spots across a range of \bar{f} .

We experimentally demonstrate this control in Sec. II. After briefly introducing the bichromatic pulses and superconducting circuit devices used in this study, we show that protection from flux noise-induced dephasing can be achieved across a significant portion of the qubit tunability band. In Sec. III, we use the flexibility offered by

*joseph@rigetti.com

Published by the American Physical Society under the terms of the [Creative Commons Attribution 4.0 International](https://creativecommons.org/licenses/by/4.0/) license. Further distribution of this work must maintain attribution to the author(s) and the published article’s title, journal citation, and DOI.

bichromatic flux modulation to improve the performance of parametric entangling gates [48–56] via sideband engineering. During a parametric gate, the frequency of a tunable qubit is modulated by an ac flux pulse to produce sidebands at multiples of the modulation frequency, centered around the time-averaged frequency \bar{f} . The use of these sidebands to activate entangling interactions with a neighboring qubit means that \bar{f} can be freely chosen, as the frequency of modulation can be adjusted to maintain resonance [57,58]. As a result, gates can be operated at any dynamical sweet spots produced by a given modulation. [46,59–61]. This freedom comes at the cost of lower effective qubit-qubit coupling, which is renormalized across all generated sidebands [62]. However, by presenting a way to alter the time dependence of a tunable qubit’s frequency during modulation, bichromatic control can be used to distribute coupling more optimally across sidebands and speed up specific interactions. Finally, in Sec. IV we highlight an example of using bichromatic sweet spot flexibility and sideband engineering to dodge gate frequency collisions.

II. DYNAMICAL SWEET SPOTS

Here we set out to demonstrate the effectiveness of bichromatic flux modulation in achieving protection against $1/f$ flux noise across a wide bandwidth of time-averaged qubit frequencies \bar{f} . We employ the following convention in parameterizing an applied flux $\Phi(t)$ involving a dc bias and two modulation frequencies:

$$\Phi(t) = \Phi_{\text{dc}} + \Phi_{\text{ac}}u(t)[\cos(\alpha)\cos(2\pi f_m t) + \sin(\alpha)\cos(2\pi p f_m t + \theta)]. \quad (1)$$

In this expression, Φ_{dc} is a dc bias amplitude, Φ_{ac} is a modulation amplitude, $u(t)$ is a waveform envelope scaled to unity, α is a mixing angle defining the relative strength of each tone, f_m is the fundamental frequency of modulation, p is a multiplier on f_m that determines the second modulation tone, and θ is a relative phase between the tones [47]. The envelope $u(t)$ is implemented as a flat-top pulse with a symmetric rise and fall described by the Gauss error function.

Two examples of bichromatic pulses defined in this way are shown in Fig. 1 along with their Fourier transforms, showing peaks in frequency content at f_m and $p f_m$ with amplitudes according to α . In-depth information regarding the generation of this class of pulses and the calibration of specific α and θ values is provided in Appendix A.

The experiments described in this paper are performed on superconducting transmons [63] within multiple 32-qubit and 40-qubit Rigetti quantum processors. All of these devices are described by the circuit diagram in Fig. 2 and

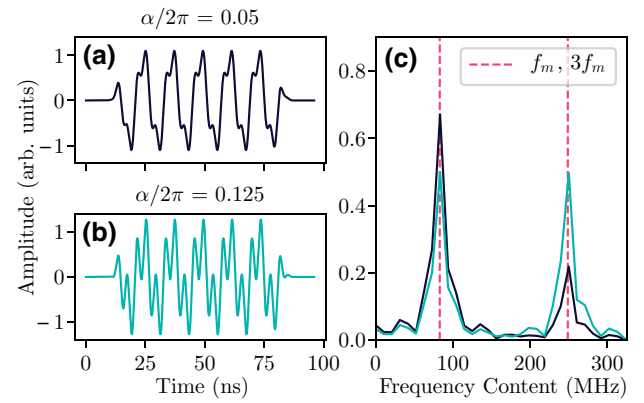


FIG. 1. (a),(b) Example waveforms described by Eq. (1). The pulses in (a) and (b) differ only in mixing angle α , sharing the following parameter values otherwise: $p = 3$, $f_m = 82.9$ MHz, $\theta/2\pi = 0.675$. (c) The Fourier transform of the pulses in (a) and (b), showing content at f_m and $3f_m$ with relative strengths dependent on α . For $\alpha/2\pi = 0.125$, displayed in teal, both tones are weighted equally.

share the properties listed in its caption. Relevant information about the specific qubits under study can be found in Table I.

To first order, the qubit dephasing rate

$$\Gamma_\phi \propto \sqrt{A_{\text{dc}}^2 \left(\frac{\partial \bar{f}}{\partial \Phi_{\text{dc}}} \right)^2 + A_{\text{ac}}^2 \left(\frac{\partial \bar{f}}{\partial \Phi_{\text{ac}}} \right)^2}, \quad (2)$$

where A_{dc} and A_{ac} are the strengths of additive and multiplicative $1/f$ noise, respectively. For experimental simplicity, we track the dephasing rate $\Gamma_2 = \Gamma_1/2 + \Gamma_\phi$, and transverse relaxation time $T_2^* = 1/\Gamma_2$, in lieu of Γ_ϕ and $T_\phi = 1/\Gamma_\phi$ because Γ_1 exhibits a comparably weak dependence on slow flux noise [59,64].

Choosing p , the frequency multiplier of the second bichromatic tone, to be an odd, positive integer ensures that $\partial \bar{f} / \partial \Phi_{\text{dc}}$ is 0 at the same biases where it is 0 without modulation [47]. In other words, for a tunable qubit with flux period Φ_0 , sweet spots that are first-order insensitive to additive flux noise persist at $\Phi_{\text{dc}} = 0$ and $\frac{1}{2}\Phi_0$ regardless of Φ_{ac} . As a result, the dc flux bias can remain constant throughout a pulse program without contributing to increased dephasing during bichromatic modulation. Another advantage of maintaining these dc sweet spots in particular is that they occur at biases around which the qubit frequency is symmetric. This symmetry eliminates odd-indexed sidebands that would otherwise be generated during modulation, cleaning the spectrum for parametric gates and leaving more renormalized coupling to be distributed amongst the remaining even sidebands (see Appendix B). To realize these benefits, all qubits in this study are biased at $\Phi_{\text{dc}} = 0$ and all bichromatic modulation uses a frequency multiplier of $p = 3$.

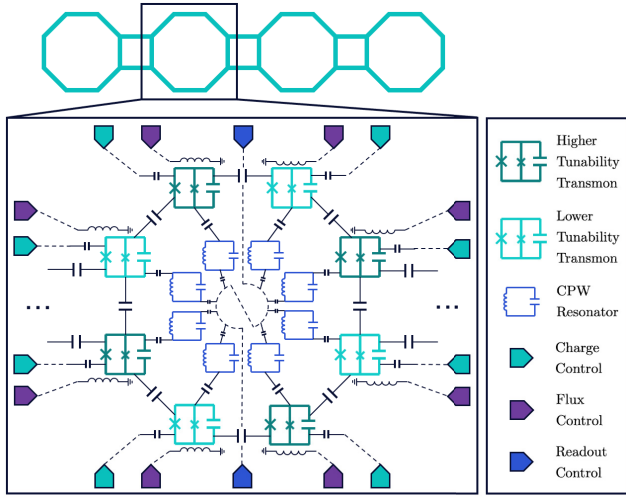


FIG. 2. A circuit diagram representation of the devices used in this study. The full lattices include either 32 or 40 tunable transmons, with the topology of eight presented here constituting an octagonal unit cell that is repeated four or five times to make up a full device. Dispersive readout is achieved via coplanar waveguide (CPW) resonators capacitively coupled to each transmon, and readout signal delivery is multiplexed eightfold by the octagon. These transmons are tunable via inductively coupled flux lines and excitable via capacitively coupled rf drive lines. There is a static capacitive coupling between each pair of neighboring qubits. The lattice alternates between two classes of transmon that differ in frequency band and tunability. Parametric gates are performed by modulating the higher frequency, higher tunability qubits and placing negative-indexed sidebands on resonance with the capacitively coupled, lower-frequency neighbors.

With $\partial\bar{f}/\partial\Phi_{dc}$ equal to 0 throughout operation, we expect T_2^* to track specifically with $\partial\bar{f}/\partial\Phi_{ac}$. At a consistent Φ_{dc} of 0, the only nonzero amplitude of monochromatic modulation in the first flux period for

which $\partial\bar{f}/\partial\Phi_{ac} = 0$ is $\Phi_{ac} \approx 0.6\Phi_0$, corresponding to a minimum in \bar{f} . This is shown in Fig. 3(a), where we measure \bar{f} and T_2^* of qubit 1 (ref. Table I) as a function of Φ_{ac} for a fixed, monochromatic modulation frequency of 300 MHz. The time-averaged frequency \bar{f} is measured with a standard Ramsey experiment by playing each flux pulse during the intervening delays between $RX(\pi/2)$ rotations. Most modulation amplitudes cause T_2^* to drop significantly, with full resurgence only measured around the dynamical sweet spot at $\Phi_{ac} = 0.6\Phi_0$ where T_2^* is approximately equal to the zero-flux value.

The additional control introduced by bichromatic modulation loosens these operating point restrictions significantly. By choosing different mixing angles α and relative phases θ , the $\partial\bar{f}/\partial\Phi_{ac} = 0$ condition can be met along a continuum of \bar{f} values within the modulated transmon's tunability band [47]. The corresponding sweet spot Φ_{ac} values are no longer fixed to $0.6\Phi_0$. We demonstrate an example of this flexibility in Fig. 3(a) by measuring qubit 1's \bar{f} and T_2^* as a function of Φ_{ac} for bichromatic modulation as well. Under this particular modulation, characterized by $\alpha/2\pi = 0.075$ and $\theta/2\pi = -0.2$, qubit 1 reaches a sweet spot at approximately $0.46\Phi_0$ that corresponds to a minimum \bar{f} about 202 MHz above the sweet spot \bar{f} achievable with monochromatic modulation. This is more directly communicated in Fig. 3(b), where the same coherence data from Fig. 3(a) are plotted as a function of \bar{f} rather than Φ_{ac} . This bichromatic modulation unlocks a new operating point protected from flux noise, allowing a fully resurgent T_2^* of 22 μs where monochromatic modulation reduces it to 5 μs .

While Fig. 3 only shows data for a single set of bichromatic modulation parameters, it is possible to extend this T_2^* resurgence across a significant portion of a qubit's tunability band by using different values of α and θ . This is demonstrated in Fig. 4 for another qubit, qubit 3 (ref. Table I). Here, by measuring coherence at various

TABLE I. Relevant information about the qubits used in the experiments described in this manuscript. Qubits 1 and 2 are capacitively coupled neighbors, as are qubits 3 and 4 and qubits 5 and 6 on different devices. The indexing labels used here are for convenience and are not representative of positioning within a lattice. The listed f_{01} values correspond to bias $\Phi_{dc} = 0$, and represent the maximum of each qubit's tunability band. Tunabilities are only listed for the qubit in each pair that is modulated to activate entangling gates. Listed anharmonicities correspond to $f_{12} - f_{01}$ at $\Phi_{dc} = 0$. Listed T_1 and T_2^* values represent coherence times measured with $\Phi_{dc} = \Phi_{ac} = 0$, when qubits are biased at their maximum frequencies and are not being modulated. Listed readout fidelities represent the average of classification probabilities $P(0|0)$ and $P(1|1)$ measured nonsimultaneously across qubits. Listed single-qubit (1Q) gate fidelities are measured with randomized benchmarking, performed nonsimultaneously across qubits.

	f_{01} (GHz)	Tunability (GHz)	Anharmonicity (GHz)	T_1 (μs)	T_2^* (μs)	Readout fidelity (%)	1Q gate fidelity (%)
Qubit 1	4.676	0.705	-0.218	21 ± 2	19 ± 2	94.6 ± 1.18	99.6 ± 0.04
Qubit 2	3.433	...	-0.202	43 ± 2	26 ± 1	94.9 ± 1.15	99.9 ± 0.04
Qubit 3	5.250	0.824	-0.205	33 ± 6	46 ± 4	96.0 ± 2.80	99.8 ± 0.01
Qubit 4	4.269	...	-0.187	25 ± 2	23 ± 4	94.2 ± 0.72	99.9 ± 0.02
Qubit 5	4.791	1.074	-0.206	25 ± 6	22 ± 2	97.0 ± 0.81	99.8 ± 0.02
Qubit 6	3.365	...	-0.201	36 ± 8	20 ± 4	92.7 ± 2.57	99.8 ± 0.01

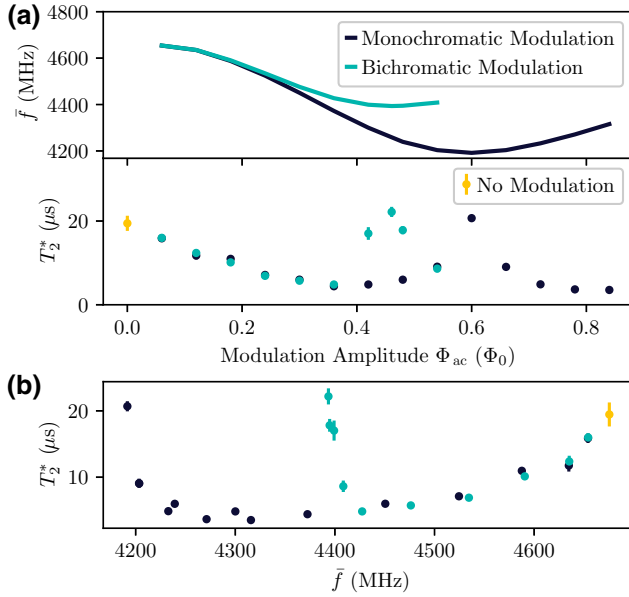


FIG. 3. (a) Measured time-averaged frequency \bar{f} and T_2^* of qubit 1 (ref. Table I) during monochromatic and bichromatic modulation, plotted as a function of modulation amplitude. This bichromatic modulation is characterized by $\alpha/2\pi = 0.075$ and $\theta/2\pi = -0.2$. The T_2^* value falls significantly at amplitudes for which \bar{f} is flux sensitive, only recovering at points where $\partial\bar{f}/\partial\Phi_{ac} = 0$. Whereas that insensitivity occurs at $0.6\Phi_0$ in the monochromatic case, this set of bichromatic parameters results in an equivalent sweet spot at $0.46\Phi_0$, corresponding to an \bar{f} that is 202 MHz above the protected monochromatic operating point. (b) The same T_2^* data as above, plotted against \bar{f} instead of modulation amplitude. This example set of bichromatic parameters can be used to greatly increase the viability of an operating point that is left unprotected from flux noise under monochromatic modulation.

dynamical sweet spots produced by different combinations of α and θ , T_2^* is held at a mean value of $27.89 \mu\text{s}$ across a 240 MHz range of \bar{f} . This same window is shown to have a ceiling of around $5 \mu\text{s}$ under monochromatic modulation, highlighting the benefit of this bichromatic control. Note that at all displayed sweet spots, this qubit consistently only reaches 61% sweet spot resurgence of the nonmodulated T_2^* value (ref. Table I). The strength of T_2^* resurgence under modulation is the subject of ongoing research [59,61].

Along those same lines, not every set of bichromatic control parameters is guaranteed to produce a sweet spot with good T_2^* resurgence, as other sources of decoherence can affect the modulated transmon. The displayed coherence times correspond to a subset of measured operating points at which resurgence is achieved. This down selection is simply performed with the intention of showing that T_2^* -resurgent sweet spots are achievable across this range of \bar{f} with at least the demonstrated density. We attribute the

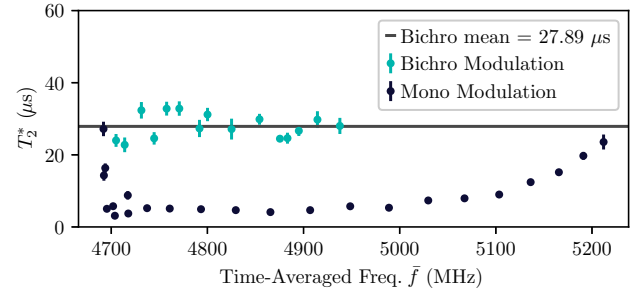


FIG. 4. The T_2^* value of qubit 3 (ref. Table I) as a function of time-averaged frequency \bar{f} during different flux modulations. The coherence times in dark blue are measured under monochromatic modulation at $f_m = 100$ MHz. The coherence times in teal are measured at sweet spots produced by bichromatic modulation of fundamental frequency $f_m = 100$ MHz and different values of mixing angle α and relative phase θ . This figure can be viewed as the best T_2^* values achievable for qubit 3 at a given \bar{f} using each type of modulation. The T_2^* resurgence at the single monochromatic sweet spot is maintainable, with at least the demonstrated operating point density, across a spectrum of bichromatic sweet spots corresponding to approximately 240 MHz of \bar{f} flexibility for this qubit.

variation in the presented T_2^* values to the defect landscape and temporal fluctuations.

III. SIDEBAND ENGINEERING FOR FASTER GATES

Maintaining qubit coherence by creating dynamical sweet spots at desired time-averaged frequencies is only one way in which bichromatic control can provide 2Q gate flexibility. Another is by optimizing sideband weights and reducing gate times, which can bring groups of otherwise prohibitively long entangling interactions into viability.

During flux modulation, sidebands of a qubit's transitions are produced at frequencies

$$f_k = \bar{f} + kf_m, \quad (3)$$

where k is the sideband index and f_m is the frequency of modulation. A native CZ interaction takes place when an f_{01} sideband is placed on resonance with a capacitively coupled neighbor's f_{12} transition frequency (or vice versa), allowing $|11\rangle \leftrightarrow |02\rangle$ swapping (or $|11\rangle \leftrightarrow |20\rangle$ swapping). Similarly, a native i SWAP interaction takes place when an f_{01} sideband is placed on resonance with a neighbor's f_{01} , allowing $|10\rangle \leftrightarrow |01\rangle$ swapping [62]. Meanwhile, the static coupling between the modulated qubit and each of its neighbors is renormalized across all generated sidebands according to their weights. This results in an effective coupling $g_{\text{eff}} = g\varepsilon_k$ for i SWAP interactions and $g_{\text{eff}} = \sqrt{2}g\varepsilon_k$ for CZ interactions, where g is the bare coupling and ε_k is the weight of the k th sideband [62]. These weights are given by the coefficient of each harmonic in

the Fourier expansion of the modulated qubit charge operator (see Appendix B). For a monochromatic gate at the sweet spot, g_{eff} is determined solely by the sideband used and cannot be dynamically tuned because all modulation parameters are fixed. However, different α and θ alter the time dependence of the qubit frequency under bichromatic modulation and can be used to tune the distribution of weight, even concentrating it into specific sidebands [47].

Figure 5(a) shows the modeled difference in achievable sideband weights using monochromatic versus bichromatic modulation to activate sweet spot CZ₀₂ interactions between qubit 5 (modulated) and qubit 6 (ref. Table I). Each bichromatic operating point has been optimized to maximize the weight of the activating sideband (see the

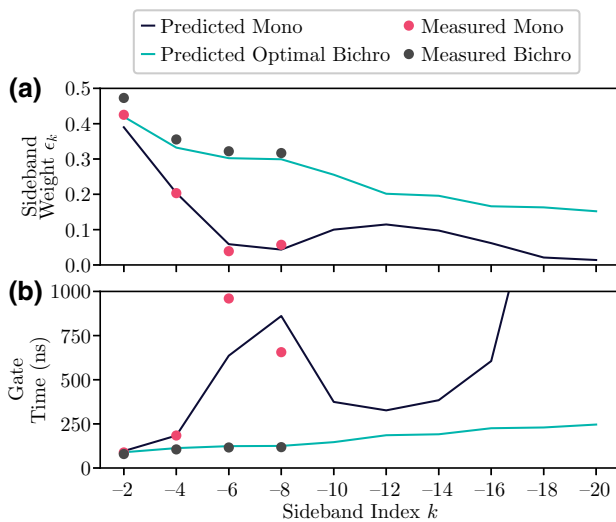


FIG. 5. (a) Predicted and measured sideband weights achievable with monochromatic and bichromatic modulation of qubit 5 (ref. Table I). All weights correspond to sweet spot flux operating points for activating a CZ₀₂ interaction with qubit 6. See Appendix B for a description of the expressions used in simulating a sideband weight for a given flux modulation. The predicted monochromatic data set is calculated in this way, using the modulation parameters corresponding to the single sweet spot interaction for each sideband. To select the optimal predicted bichromatic weight for a given sideband, modulation amplitude Φ_{ac} is swept from $0.1\Phi_0$ to $0.9\Phi_0$ and mixing angle α is swept from 0 to $\pi/2$. For each pair of Φ_{ac} and α , a relative phase θ is calculated that would create a sweet spot at Φ_{ac} if possible. For each of these operating points, we then calculate average detuning, required modulation frequency, and finally sideband weight and gate time according to the expressions in Appendix B. The operating point with the fastest predicted gate time is selected for each sideband, and the measured weights are extracted from the measured gate times at these operating points. (b) The predicted and measured gate times associated with the sidebands described in panel (a). In general, bichromatic operating points can be optimized to concentrate weight into the gate-activating sideband, dramatically reducing obtainable gate times at higher sideband indices.

caption of Fig. 5 for details). Only even-index sidebands are shown because qubit 5 is biased at the maximum of its tunability band for the scope of this study, and the symmetry of modulation around this parking frequency reduces the odd Fourier coefficients to 0. The trend in monochromatic weights is typical in that they oscillate downward with increasing sideband index, eventually vanishing. Comparatively, the optimized weights produced by specific bichromatic pulse parameters are similar for $k = -2$ but drop off less quickly with index. This leads to significant reductions in predicted gate times, which are inversely proportional to sideband weights and are displayed in Fig. 5(b).

For monochromatic and bichromatic gates at each of the predicted operating points up through the -8 th sideband, measured gate times and extracted sideband weights are plotted over the model results in Fig. 5. We find good agreement for the sidebands with weights above 0.1, measuring increasingly long monochromatic CZ gates and relatively constant-duration bichromatic CZ gates with increasing sideband index. For the more weakly weighted monochromatic $k = -6$ and $k = -8$ sidebands, small errors in predicted weight create larger discrepancies in gate times. That being said, these gates are found to be significantly longer than their bichromatic counterparts.

The population exchange of qubit 6 during two $k = -8$ CZ₀₂ interactions with qubit 5 is shown in Fig. 6, with the monochromatic sweet spot operating point in panel (a) and a faster bichromatic sweet spot operating point in panel (b). While the activating fundamental modulation frequencies are only about 8.5 MHz apart, the difference in \tilde{f} is 8 times that due to the sideband being used. The bichromatic operating point provides a factor of 4 speed-up as well as a corresponding boost in interleaved randomized benchmarking fidelity, from $92.7\% \pm 2.15\%$ for the monochromatic gate to $98.8\% \pm 0.50\%$ for the bichromatic. Measurements of coherence during modulation show the fidelity of both gates to be coherence limited within uncertainty [46,61].

As a result of differing modulation frequency requirements for specific interactions, some modulated qubits have an even more dramatic reduction in monochromatic gate sideband weight as the index increases. For example, the monochromatic $k = -4$ CZ₀₂ gates between qubits 1 and 2 (ref. Table I) has a measured gate duration of approximately $2.844 \mu\text{s}$. Even with the full T_2^* resurgence qubit 1 is shown to exhibit at sweet spots in Fig. 3, such a long gate time results in a coherence-limited fidelity well below 90%. Again, this coherence limit can be significantly improved by optimizing the $k = -4$ sideband with bichromatic modulation. Figure 7 shows four examples of $k = -4$ CZ₀₂ operating points at bichromatic sweet spots for qubits 1 and 2, spanning 170 MHz in qubit 1 average frequency. These gates demonstrate 7–10 times reductions in gate time relative to the monochromatic equivalent, and

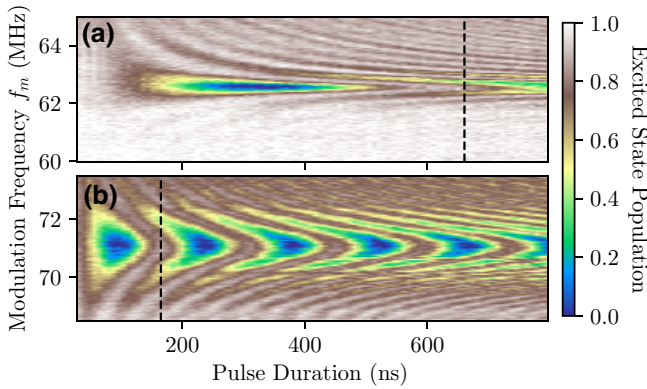


FIG. 6. Excited state population of qubit 6, undergoing $|1\rangle \leftrightarrow |0\rangle$ transfer during a CZ interaction mediated by the $k = -8$ sideband of qubit 5's f_{12} transition frequency. Population exchange at each resonance condition is visualized by sweeping pulse duration and fundamental modulation frequency for constant modulation amplitude at the respective sweet spot. Panel (a) features the monochromatic instance of this gate, while panel (b) features a bichromatic operating point selected for increased sideband weight ε_{-8} (not the same operating point featured in Fig. 5, which has lower fidelity due to a collision). The frequency axes of both panels have the same scale, highlighting the relative resonance widths that scale with coupling strength. The black dotted lines correspond to fit durations of a full CZ interaction, showing a bichromatic speed-up by almost exactly a factor of 4 after pulse risetimes are included in total duration. The bichromatic gate has an interleaved randomized benchmarking fidelity of $98.8\% \pm 0.50\%$, compared to the $92.7\% \pm 2.15\%$ fidelity of the monochromatic gate.

they have largely coherence-limited fidelities averaging to just below 98% via interleaved randomized benchmarking.

While the fastest gates under study are still found with the $k = -2$ sideband, the ability to significantly increase the effective coupling for higher-order sidebands is not without benefit. Used for this purpose, bichromatic modulation can unlock both additional \bar{f} flexibility and entangling interactions for which f_m would otherwise be limited by arbitrary waveform generator (AWG) bandwidth.

IV. DODGING COLLISIONS

The freedom to select a specific \bar{f} for a modulated qubit is advantageous for dodging collisions in two ways. First and most directly, any unintended coupling with two-level system defects [1–7] or other qubits near \bar{f} at the monochromatic sweet spot can be avoided. Second, \bar{f} can be chosen to avoid similar spurious interactions involving any of the generated sidebands. The fixed, monochromatic sweet spot \bar{f} also fixes the modulation frequency required to place a given sideband on resonance with a neighboring qubit to activate an entangling interaction. In the event that any other sidebands generated with this modulation frequency collide with TLS or the resonance

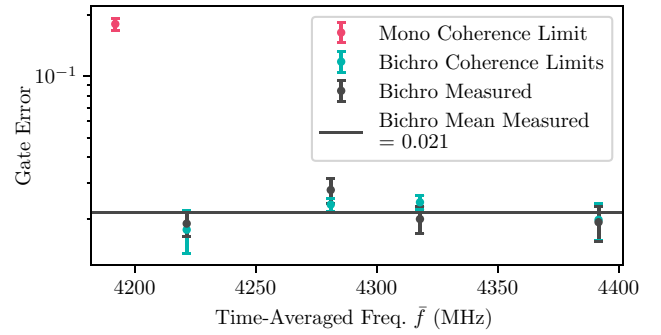


FIG. 7. The measured gate error and coherence-limited error for four bichromatic, $k = -4$ CZ_{02} gates between qubits 1 and 2 (ref. Table I), plotted against the time-averaged frequency of qubit 1 during modulation. The calculated coherence limit for the monochromatic $k = -4$ CZ_{02} gate is included for comparison. Each gate is operated at a dynamical sweet spot, and each measured point is the weighted mean of six or more measurements of gate error and coherence-limited error. Error bars represent the standard deviations of these distributions. Gate errors are measured via interleaved randomized benchmarking, and the bichromatic coherence limits are calculated by directly measuring coherence times under each bichromatic modulation. The monochromatic coherence limit is calculated using the coherence times in Table I with a best-case assumption of 100% sweet spot resurgence (demonstrated in Fig. 3 for this qubit) during modulation at this gate operating point. Even under these assumptions for the monochromatic gate, there is an order-of-magnitude difference between bichromatic and monochromatic coherence limits resulting from the 7–10 times shorter bichromatic gate times. Details about these operating points can be found in Table II.

condition of a different gate, population is lost from the intended exchange and fidelity drops accordingly. While the modulation frequency is still fixed for a given \bar{f} in the bichromatic case, the value of \bar{f} can be tuned to ensure collision-free sidebands.

It is worth emphasizing that, by leaving the sweet spot, it is possible to use monochromatic modulation to attain most (but not all) of the \bar{f} band available at bichromatic sweet spots. However, doing so comes at a significant cost to both T_2^* (see Fig. 3) and gate stability over time. The advantage of bichromatic modulation is not necessarily the attainability of these \bar{f} values, but rather the attainability of these \bar{f} values at operating points protected from slow flux noise.

Here we focus on qubits 3 and 4 (ref. Table I), for which a sideband collision at the sweet spot limits fidelity in the monochromatic case. This pair's various resonance conditions for the $k = -2$ and $k = -4$ sidebands produced by monochromatic modulation are shown in Fig. 8(a). At the sweet spot ($\Phi_{ac} \approx 0.6\Phi_0$), the $k = -2$ CZ_{02} interaction collides with the $k = -4$ i SWAP interaction. While the $k = -2$ sideband has significantly more weight and the $|11\rangle \leftrightarrow |02\rangle$ transfer will happen more quickly as a result,

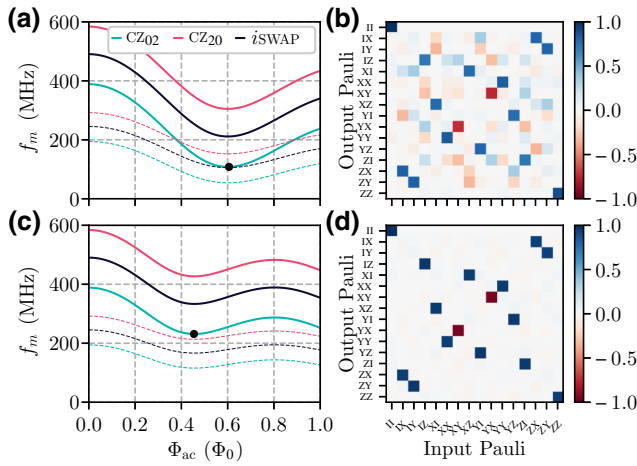


FIG. 8. (a) Monochromatic modulation frequencies for activating native entangling gates between qubits 3 and 4 (ref. Table I) with the $k = -2$ (solid lines) and $k = -4$ (dashed lines) sidebands at different modulation amplitudes. A collision is found between the $k = -2$ CZ₀₂ and $k = -4$ *i*SWAP interactions at the sweet spot. (b) Measured process map for the optimized monochromatic CZ₀₂ pulse, generated via process tomography. Strong XY-like terms are introducing coherent error. (c) Resonance conditions for the same edge, but under bichromatic modulation with $\alpha/2\pi = 0.085$ and $\theta/2\pi = -0.06$. The corresponding shift in \bar{f} resolves the gate collision. (d) Measured process map for the optimized bichromatic CZ₀₂ pulse, revealing a much cleaner approximation of the ideal CZ operator.

cutting off the interaction at the ideal time for the CZ gate still produces an operation that involves a strong XY-like swapping [see the process map in Fig. 8(b) [65–67]]. This CZ operation has a fidelity of $90.0\% \pm 2.60\%$, as measured by interleaved randomized benchmarking [68,69].

However, a change in \bar{f} can improve this fidelity. If \bar{f} is shifted by a value Δ then the modulation frequency required to activate $k = -2$ interactions moves by $\Delta/2$ while the frequency required for $k = -4$ interactions only moves by $\Delta/4$, according to Eq. (3). Using bichromatic modulation of $\alpha/2\pi = 0.085$ and $\theta/2\pi = -0.06$, the sweet spot modulation amplitude is reduced by about 25% and the corresponding \bar{f} is shifted up by $\Delta \approx 234$ MHz. The resulting collision-free set of resonance conditions is shown in Fig. 8(c), along with a much cleaner process map for the calibrated CZ gate in Fig. 8(d). Gate error is reduced by a factor 5 from the monochromatic case, reaching an interleaved randomized benchmarking fidelity of $98.0\% \pm 0.28\%$.

Of course, this particular set of bichromatic parameters is not unique in its ability to dodge the gate collision that limits monochromatic fidelity. Like Fig. 7 shows for qubits 1 and 2, as long as no new collisions are introduced or gate time is not significantly lengthened at a specific operating point, \bar{f} can be placed anywhere across the attainable bichromatic sweet spot band. By simulating the detuning

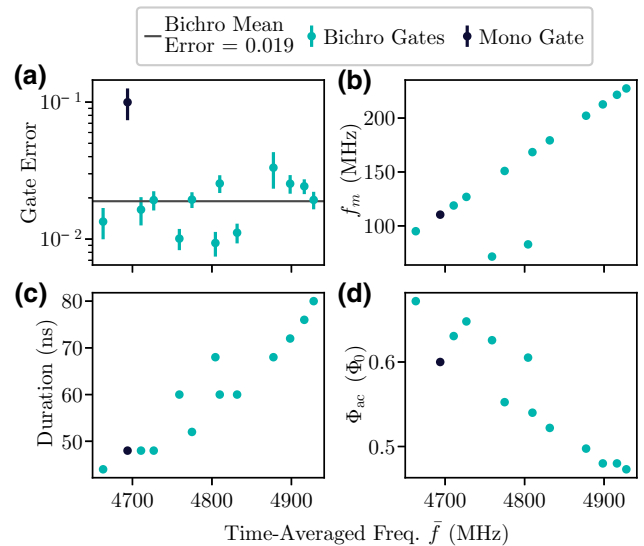


FIG. 9. (a) The gate error for 12 bichromatic CZ₀₂ gates between qubit 3 and qubit 4, measured via interleaved randomized benchmarking and plotted against the time-averaged frequency of qubit 1 during modulation. The gates include both $k = -2$ and $k = -4$ sideband interactions, all operated at dynamical sweet spots. The $k = -2$ gate at the single monochromatic sweet spot is included for comparison. The monochromatic $k = -4$ gate is not brought up due to the required f_m being too low for the filtration scheme in use. (b) Modulation frequencies f_m for each operating point. The distinct linear sets correspond to the two sidebands being used to activate the gates [see Eq. (3)]. (c) Gate times for the full set of operating points. The native CZ₀₂ interaction involves two full $|11\rangle \leftrightarrow |02\rangle$ swaps, the rate of which is determined by the weight of the activating sideband. (d) Modulation amplitudes Φ_{ac} , all of which satisfy the dynamical sweet spot condition $\partial\bar{f}/\partial\Phi_{ac} = 0$ for each set of bichromatic modulation parameters. Details about these operating points can be found in Table III.

expected for modulation of various α and θ , gates can be found at specific, desirable values of \bar{f} or modulation frequencies f_m . See Appendix A for details concerning pulse calibration and obtaining agreement with simulations like this.

A set of CZ₀₂ gates between qubits 3 and 4 operated across a range of bichromatic operating points is shown in Fig. 9. All of these gates are operated at sweet spots and the corresponding average frequencies of qubit 3 span a range of 264 MHz. Via interleaved randomized benchmarking, this set of gates is found to reach a mean fidelity of just over 98%, with individual gates as high as $99.0\% \pm 0.19\%$.

Again, it is worth noting that these fidelities are certainly not achievable at every sweet spot in the available continuum, as there are many such operating points that suffer from collisions just like the monochromatic gate, or that result in poor weighting of the activating sideband. To further this point, unlike the gates in Sec. III, these gates do not reach the coherence limits that can be assumed from

the T_2^* resurgence levels of qubit 3 in Fig. 4. The fidelity of this gate set is likely limited by loss of population as qubit 3 moves through resonance with two-level system defects during the rise and fall times of each flux pulse. Regarding coherence measurements, this phenomenon manifests as small reductions in the amplitude of exponential fits rather than as reductions in the coherence times themselves. Quantification and mitigation of this source of error are the subjects of ongoing research. Figure 9 is meant only to communicate a lower bound on the density with which gates of at least these fidelities can be brought up. Even when coherence does not limit a two-qubit gate's fidelity, the ability to operate at a dynamical sweet spot is still vital for stability in the face of flux pulse amplitude drift over time. In general, this flexibility in operating point represents a significant advantage in robustness over the single monochromatic sweet spot, and will only become more useful as higher lattice connectivity introduces more frequency crowding.

V. CONCLUSION

We have experimentally verified that bichromatic flux modulation can be used to extend the range of time-averaged frequencies accessible to tunable transmons at operating points protected from slow flux noise. We have demonstrated the usefulness of this freedom for reducing two-qubit parametric gate error, both by reducing gate speed with improved sideband weights and dodging unwanted collisions.

A promising application of bichromatic flux control left to future work is parametric-resonance gates, which have recently been implemented on a tunable-coupler architecture [70]. To perform these gates, the average frequency of a modulated qubit is brought directly onto resonance with a neighbor. With the frequency of modulation no longer relevant for activating the gate, it can be optimized independently to avoid collisions. Moreover, the weight of the activating $k = 0$ sideband can reach values close to unity, allowing fast gates at the bare coupling rate. Bichromatic control would allow these gates to be implemented at dynamical sweet spots, presenting the opportunity to increase their fidelity substantially [47].

In summary, the flexibility provided by this novel control technique represents an important step forward in terms of robustness to experimental imperfection as well as scalability of flux-tunable qubit architectures. As such, bichromatic flux modulation is shown to be a promising method for achieving controlled entanglement on superconducting processors.

ACKNOWLEDGMENTS

We thank Prasahnt Sivarajah and Deanna Abrams for their initial exploration of calibrating bichromatic pulses. We thank Gregory Stiehl and Alexander Hill for helpful

discussions and for critically reading the manuscript. We thank Ben Scharmann for his help in designing the device Hamiltonians under study. Finally, we thank all of our collaborators at Rigetti Computing, without whose effort the computing stack used in this study would not exist.

The experimental results presented here are based upon work supported by the Defense Advanced Research Projects Agency (DARPA) under Agreement No. HR00112090058.

J.A.V. drafted the manuscript. S.C., N.D., and J.A.V. performed the initial validation of theory. J.A.V. implemented the measurement tools and performed the experiments. N.D. developed the theory describing bichromatic flux control of tunable transmons and created simulation tools used in the study. G.J. organized the construction of the control systems in use, and provided critical knowledge and support throughout the study. N.D. organized the experimental effort.

APPENDIX A: PULSE CALIBRATION

In achieving the various results discussed in this paper, the bichromatic pulses defined in Sec. II are produced in two ways. The first, simpler method is via a single field programmable gate array (FPGA)-based sequencer. The modulation waveform containing both frequencies of the bichromatic pulse is precomputed as a single set of digital values that are fed into a DAC. This scheme is sufficient for many experiments, but requires some additional considerations that are described here.

It is normally convenient, for the sake of tracking phase, to define control pulses relative to local rotating frames that oscillate at some characteristic frequency of the system. Doing so imparts a global frame phase on those pulses, which is usually irrelevant but introduces complications for bichromatic pulses produced by a single sequencer with two frequencies in the baseband waveform. Specifically, the effective value of θ is shifted by $1 - p$ times the applied phase.

To understand this, consider a simplified version of the ac pulse in Eq. (1) with a global phase shift β :

$$\begin{aligned} \Phi(t) = & \cos(\alpha) \cos(2\pi f_m t + \beta) \\ & + \sin(\alpha) \cos(2\pi p f_m t + \theta + \beta). \end{aligned} \quad (\text{A1})$$

To reorganize into the conventional format of a single relative phase on the second tone, we can advance the clock by $\beta/(2\pi f_m)$, the amount of time it takes the oscillation of the first tone to cycle through β . With $t' = t + \beta/(2\pi f_m)$, we can re-express Eq. (A1) as

$$\begin{aligned} \Phi(t') = & \cos(\alpha) \cos(2\pi f_m t') \\ & + \sin(\alpha) \cos(2\pi p f_m t' + \theta + (1 - p)\beta). \end{aligned} \quad (\text{A2})$$

In this form, it becomes clear that the β phase shift has produced a new effective relative phase between the tones,

$\theta' = \theta + (1 - p)\beta$. In terms of precompensation, the used θ should be $(p - 1)\beta$ greater than the desired θ .

Another way to understand this is that every phase shift β of the f_m tone should correspond to a phase shift $p\beta$ of the pf_m tone if the relative phase between the tones is to be preserved. When both tones are shifted by β , there is a $(p - 1)\beta$ difference to make up.

In the case of a global phase coming from a rotating frame on which a bichromatic pulse is defined, the necessary θ precompensation is inconvenient because the applied shift will change depending on when a pulse is played in a program. As a result, producing repeatable bichromatic pulses with one sequencer lends itself to foregoing a rotating frame completely and instead defining the bichromatic modulation tones relative to the lab frame. This eliminates the global phase and the overhead involved in redefining pulses based on a tracked frame phase throughout a program.

While this is a tractable (and even simplifying) solution to use with CZ gates, it is not sufficient for the single-pulse decomposition scheme used by Rigetti to perform arbitrary gates in the CPHASE and XY families [60]. This strategy requires the ability to parametrically compile gates such that only waveform phase shifts are needed to control entangling angles [71]. Additionally, XY gates in particular benefit from specific, nonzero frame frequencies that greatly simplify the calibration of their entangling phase. For those reasons, we introduce the second method of producing bichromatic pulses: using two FPGA-based sequencers per flux control port, one for each harmonic. The two output signals are digitally summed before being sent to a single DAC, enabling individual frame control for each tone in the pulse. In this configuration, phase shifts on the combined waveform can be implemented with a simple scaling of the harmonic tone's shift by the bichromatic frequency ratio p .

However, both methods leave an additional phase in need of calibration, and that is the relative phase between the FPGA clock and local oscillator (LO) within each waveform generator. This becomes another global phase shift on the bichromatic waveform (not properly scaled for the harmonic tone in the two-sequencer scheme), which we denote θ_0 . It is possible to keep θ_0 constant throughout a circuit by ensuring all pulse programs start on integer multiples of both the FPGA clock cycle and the LO period. Under this condition, θ_0 just needs to be calibrated once per AWG in order to accurately produce specific values of θ in applied flux of the following form:

$$\Phi(t) = \Phi_{dc} + \Phi_{ac}u(t)[\cos(\alpha)\cos(2\pi f_m t) + \sin(\alpha)\cos(2\pi p f_m t + \theta + (1 - p)\theta_0)]. \quad (\text{A3})$$

The constant phase offset can be measured by sweeping θ for modulation of constant Φ_{ac} and measuring the induced detuning, which will have sinusoidal dependence on θ with

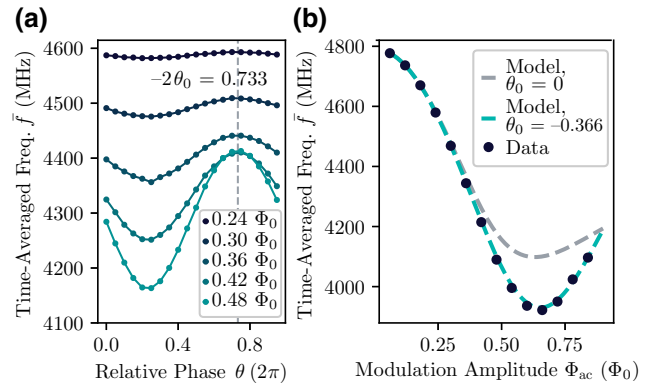


FIG. 10. (a) Measurement of θ_0 for qubit 3. For bichromatic modulation of constant p , α , and amplitude Φ_{ac} , time-averaged qubit frequency \tilde{f} is sinusoidal in $\theta + (1 - p)\theta_0$. The phase offset of the fitted \tilde{f} oscillation in θ can thus be mapped to θ_0 . While one Φ_{ac} is sufficient to measure this offset, the fit value here is the median of offsets measured at five different modulation amplitudes. (b) For the same qubit, measured detuning under bichromatic modulation is compared against model predictions that do and do not take into account the measured θ_0 . The models agree at low modulation amplitudes, which can also be seen in panel (a) in the form of smaller fluctuations in \tilde{f} at smaller Φ_{ac} . Close to the sweet spot however, θ_0 corresponds to a predicted detuning difference of about 183 MHz. The data match the model that incorporates the measured θ_0 value, illustrating the importance of this calibration for experimental realization of predicted behavior.

an offset of $(1 - p)\theta_0$ (See Appendix B). Average qubit detuning during modulation is measured with a Ramsey-style experiment in which each flux pulse is continually delivered during the delay times between $RX(\pi/2)$ rotations. Figure 10(a) shows the results of one such calibration measurement for qubit 3 (ref. Table I), while Fig. 10(b) communicates the importance of accurately measuring and accounting for θ_0 when attempting to reconcile the model and data.

We have verified these calibrations to be stable in time on the order of at least weeks in our setup. However, it is worth noting that if restarting an AWG randomizes the clock-oscillator phase, it becomes necessary to remeasure θ_0 in order to restore model agreement.

Regarding the mixing angle α , achieving a desired value requires compensation for any frequency-dependent attenuation present in the flux line. The calibration of this transfer function is performed with the same flux-Ramsey procedure described above, where the different detunings caused by monochromatic modulation at different frequencies are used to determine corrective scaling factors. With the frequency-dependent transmission flattened to a single reference value in this way, knowledge of the relationship between the sourced amplitude and Φ_0 at that reference transmission allows specific flux operating points to be realized. An example transfer function can be found in

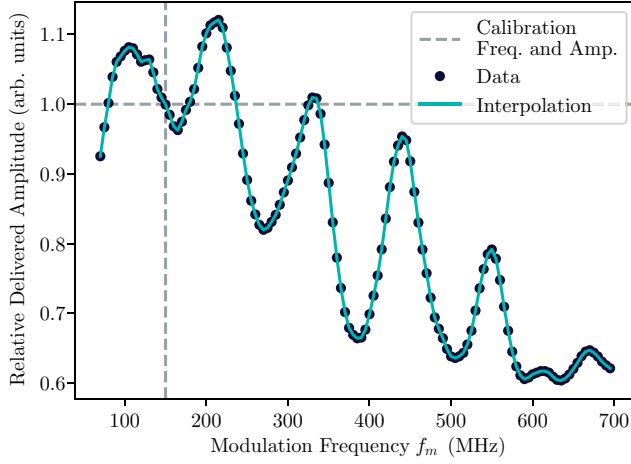


FIG. 11. An example amplitude transfer function of a flux transmission line, for qubit 5 in this case (ref. Table I). At each frequency, the effective modulation amplitude seen by the qubit is determined by measuring the detuning of the qubit frequency. The strong frequency dependence of the transfer function can then be compensated for by scaling flux pulses according to their frequency and its measured relative transmission.

Fig. 11. In the construction of bichromatic pulses, the amplitude of each tone must be scaled appropriately for its frequency before the tones are digitally added together.

APPENDIX B: TRANSMON UNDER BICHROMATIC MODULATION

The properties of a tunable transmon are controlled with magnetic flux applied on a SQUID loop by changing the effective Josephson energy

$$E_{J,\text{eff}} = \sqrt{E_{J,1}^2 + E_{J,2}^2 + 2E_{J,1}E_{J,2} \cos(\phi)}. \quad (\text{B1})$$

Here, $\phi = 2\pi \Phi / \Phi_0$ and $E_{J,1}, E_{J,2}$ are the Josephson energies of the SQUID loop. The transition frequencies are Φ_0 periodic, symmetric around zero flux bias, and can be

expressed as the Fourier series

$$f(\phi) = \sum_{n=0}^{\infty} F_n \cos(n\phi). \quad (\text{B2})$$

Under a bichromatic modulation $\Phi(t) = \Phi_{\text{dc}} + \Phi_{\text{ac}1} \cos(2\pi f_m t + \theta_1) + \Phi_{\text{ac}p} \cos(2\pi p f_m t + \theta_p)$, the time-averaged transmon frequency is equal to

$$\begin{aligned} \bar{f} &= \sum_{m=0}^{\infty} v_m \cos(m\theta), \\ v_m &= \sum_{n=0}^{\infty} F_n \cos \left[n\phi_{\text{dc}} + (p+1)m \frac{\pi}{2} \right] \\ &\times (2 - \delta_{m,0}) J_{pm}(n\phi_{\text{ac}1}) J_m(n\phi_{\text{ac}p}), \end{aligned} \quad (\text{B3})$$

which is 2π periodic in $\theta = \theta_p - p\theta_1$. Given this symmetry, we choose the convention $\theta_1 = 0$ in defining bichromatic pulses throughout the study.

In the transmon basis, the qubit-qubit coupling is flux dependent. Under modulation, the effective coupling activated by the k th sideband is $g_k = g\varepsilon_k$, renormalized from the zero-flux bare coupling g by the sideband weight ε_k . These weights are obtained from

$$g_k = \frac{1}{T_m} \int_0^{T_m} dt g(\Phi(t)) e^{i2\pi \int_0^t dt' f(\Phi(t'))} e^{-i2\pi(\bar{f} + kf_m)t}, \quad (\text{B4})$$

where $T_m = 1/f_m$ is the modulation period.

Throughout the experiments described in this study, $\Phi_{\text{dc}} = 0$ and p is odd. The bichromatic modulation is then $T_m/2$ antiperiodic, and because the effective Josephson energy [Eq. (B1)] is an even function of the flux bias, the transmon parameters oscillate at twice the modulation frequency. As a consequence, only the even sidebands are generated.

Moreover, for $p = 3$, the dependence of the average frequency on the dc bias in Eq. (B3) simplifies to $\cos(n\phi_{\text{dc}})$. Its derivative vanishes at $\Phi_{\text{dc}} = 0$, thereby protecting the transmon from slow additive flux noise during modulation.

TABLE II. Information about the CZ₀₂ operating points and gates presented in Sec. III and Fig. 7, listed in order of qubit 1's \bar{f} . All of these operating points represent dynamical sweet spots with first-order protection against $1/f$ flux noise. An exact monochromatic fidelity is not provided due to low signal to noise in the interleaved randomized benchmarking procedure, which is ill suited to measuring such low fidelities.

Sideband index k	Frequency multiplier p	Mixing angle $\alpha (2\pi)$	Relative phase $\theta (2\pi)$	Time-averaged frequency \bar{f} (MHz)	Modulation frequency f_m (MHz)	Interaction time (ns)	Modulation amplitude $\Phi_{\text{ac}} (\Phi_0)$	Gate fidelity (%)
-4	1	0.000	0.000	4192	135.04	2844	0.6	< 90.0
-4	3	0.110	0.300	4222	142.42	212	0.59	98.1 ± 0.26
-4	3	0.110	0.420	4281	157.31	292	0.59	97.2 ± 0.39
-4	3	0.105	0.525	4318	166.52	348	0.58	98.0 ± 0.3
-4	3	0.075	-0.18	4392	184.98	260	0.47	98.1 ± 0.37

TABLE III. Information about the CZ_{02} operating points and gates presented in Sec. IV and Fig. 9, listed in order of qubit 3's \bar{f} . All of these operating points represent dynamical sweet spots with first-order protection against $1/f$ flux noise.

Sideband index k	Frequency multiplier p	Mixing angle α (2π)	Relative phase θ (2π)	Time-averaged frequency \bar{f} (MHz)	Modulation frequency f_m (MHz)	Interaction time (ns)	Modulation amplitude Φ_{ac} (Φ_0)	Gate fidelity (%)
-2	3	0.005	0.570	4663	95.04	44	0.67	98.6 ± 0.34
-2	1	0.000	0.000	4694	110.41	48	0.60	90.0 ± 2.60
-2	3	0.005	0.045	4711	118.88	48	0.63	98.3 ± 0.38
-2	3	0.015	0.210	4727	126.87	48	0.65	98.0 ± 0.31
-4	3	0.015	0.200	4759	71.50	60	0.63	98.9 ± 0.18
-2	3	0.020	-0.050	4775	150.93	52	0.55	98.0 ± 0.26
-4	3	0.025	0.150	4804	82.84	68	0.61	99.0 ± 0.19
-2	3	0.035	-0.100	4810	168.42	60	0.54	97.4 ± 0.38
-2	3	0.035	0.000	4832	179.33	60	0.52	98.8 ± 0.18
-2	3	0.050	-0.045	4877	202.17	68	0.50	96.6 ± 0.99
-2	3	0.060	-0.032	4898	212.70	72	0.48	97.4 ± 0.39
-2	3	0.075	-0.056	4916	221.59	76	0.48	97.5 ± 0.30
-2	3	0.085	-0.060	4928	227.49	80	0.47	98.0 ± 0.28

APPENDIX C: GATE INFORMATION

For reference, included in Table II are details regarding the monochromatic and bichromatic operating points used to perform the gates presented in Fig. 7. Table III contains the same information for the gates presented in Fig. 9. An example instance of interleaved randomized benchmarking for one of these gates can be seen in Fig. 12, along with implementation details in the caption [68,69]. All fidelities cited in this manuscript are measured using this same protocol.

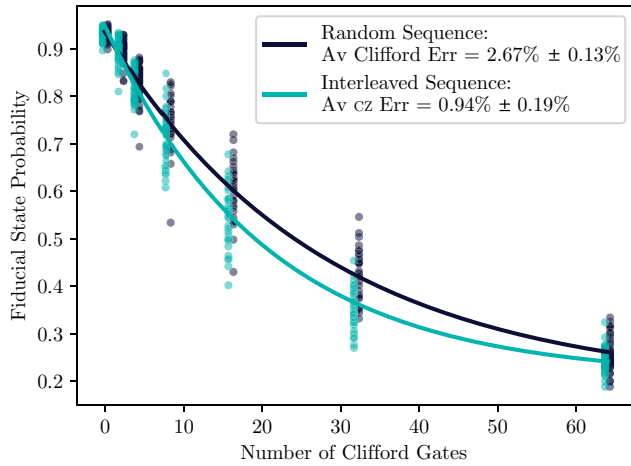


FIG. 12. An example of the interleaved randomized benchmarking data used to produce the fidelities in Tables II and III. These particular data correspond to the gate in Table III during which qubit 3's average frequency $\bar{f} = 4804$ MHz. Thirty-two trials are run for each sequence length of 0, 2, 4, 8, 16, 32, and 64 Clifford gates. Individual data points correspond to the average probability of reading out the fiducial state over 500 shots per trial.

- [1] J. M. Martinis, K. B. Cooper, R. McDermott, M. Steffen, M. Ansmann, K. D. Osborn, K. Cicak, S. Oh, D. P. Pappas, R. W. Simmonds, and C. C. Yu, Decoherence in Josephson Qubits from Dielectric Loss, *Phys. Rev. Lett.* **95**, 210503 (2005).
- [2] C. Müller, J. Lisenfeld, A. Shnirman, and S. Poletto, Interacting two-level defects as sources of fluctuating high-frequency noise in superconducting circuits, *Phys. Rev. B* **92**, 035442 (2015).
- [3] P. V. Klimov *et al.*, Fluctuations of Energy-Relaxation Times in Superconducting Qubits, *Phys. Rev. Lett.* **121**, 090502 (2018).
- [4] J. J. Burnett, A. Bengtsson, M. Scigliuzzo, D. Niepce, M. Kudra, P. Delsing, and J. Bylander, Decoherence benchmarking of superconducting qubits, *Npj Quantum Inf.* **5**, 54 (2019).
- [5] S. Schlör, J. Lisenfeld, C. Müller, A. Bilmes, A. Schneider, D. P. Pappas, A. V. Ustinov, and M. Weides, Correlating Decoherence in Transmon Qubits: Low Frequency Noise by Single Fluctuators, *Phys. Rev. Lett.* **123**, 190502 (2019).
- [6] J. Lisenfeld, A. Bilmes, A. Megrant, R. Barends, J. Kelly, P. Klimov, G. Weiss, J. M. Martinis, and A. V. Ustinov, Electric field spectroscopy of material defects in transmon qubits, *Npj Quantum Inf.* **5**, 105 (2019).
- [7] A. Bilmes, A. Megrant, P. Klimov, G. Weiss, J. M. Martinis, A. V. Ustinov, and J. Lisenfeld, Resolving the positions of defects in superconducting quantum bits, [arXiv:1911.08246](https://arxiv.org/abs/1911.08246) (2019).
- [8] T. Lehnert, D. Billon, C. Grassl, and K. H. Gundlach, Thermal annealing properties of Nb-Al/AIO_x-Nb tunnel junctions, *J. Appl. Phys.* **72**, 3165 (1992).
- [9] A. Oliva and R. Monaco, Annealing properties of high quality Nb/Al-AIO_x/Nb tunnel junctions, *IEEE Trans. Appl. Supercond.* **4**, 25 (1994).
- [10] A. Potts, G. Parker, J. Baumberg, and P. Groot, Cmos compatible fabrication methods for submicron Josephson

- junction qubits, *Sci. Meas. Technol. IEE Proc.* **148**, 225 (2001).
- [11] P. Koppinen, L. M. Vaisto, and I. Maasilta, Complete stabilization and improvement of the characteristics of tunnel junctions by thermal annealing, *Appl. Phys. Lett.* **90**, 053503 (2007).
- [12] C. Granata, A. Vettoliere, L. Petti, M. Ripa, B. Ruggiero, P. Mormile, and M. Russo, Trimming of critical current in niobium Josephson devices by laser annealing, *J. Phys.: Conf. Ser.* **97**, 012110 (2008).
- [13] B. Bumble, A. Fung, A. Kaul, A. W. Kleinsasser, G. L. Kerber, P. Bunyk, and E. Ladizinsky, Submicrometer Nb/Al-AIO_x/Nb integrated circuit fabrication process for quantum computing applications, *IEEE Trans. Appl. Supercond.* **19**, 226 (2009).
- [14] I. Pop, T. Fournier, T. Crozes, F. Lecocq, I. Matei, B. Panetier, O. Buisson, and W. Guichard, Fabrication of stable and reproducible submicron tunnel junctions, *J. Vac. Sci. Technol. B* **30**, 010607 (2012).
- [15] M. V. Costache, G. Bridoux, I. Neumann, and S. O. Valenzuela, Lateral metallic devices made by a multiangle shadow evaporation technique, *J. Vac. Sci. Technol. B* **30**, 04E105 (2012).
- [16] X. Wu, J. L. Long, H. S. Ku, R. E. Lake, M. Bal, and D. P. Pappas, Overlap junctions for high coherence superconducting qubits, *Appl. Phys. Lett.* **111**, 032602 (2017).
- [17] M. Brink, J. Chow, J. Hertzberg, E. Magesan, and S. Rosenblatt, *2018 IEEE International Electron Devices Meeting (IEDM)*, 6.1.1 (2018).
- [18] J. M. Kreikebaum, K. P. O'Brien, A. Morvan, and I. Siddiqi, Improving wafer-scale Josephson junction resistance variation in superconducting quantum coherent circuits, *Supercond. Sci. Technol.* **33**, 06LT02 (2020).
- [19] C. Dickel, J. J. Wesdorp, N. K. Langford, S. Peiter, R. Sagastizabal, A. Bruno, B. Criger, F. Motzoi, and L. DiCarlo, Chip-to-chip entanglement of transmon qubits using engineered measurement fields, *Phys. Rev. B* **97**, 064508 (2018).
- [20] K. S. Chou, J. Z. Blumoff, C. S. Wang, P. C. Reinhold, C. J. Axline, Y. Y. Gao, L. Frunzio, M. H. Devoret, L. Jiang, and R. J. Schoelkopf, Deterministic teleportation of a quantum gate between two logical qubits, *Nature* **561**, 368 (2018).
- [21] Y. Zhong, H.-S. Chang, A. Bienfait, É. Dumur, M.-H. Chou, C. R. Conner, J. Grebel, R. G. Povey, H. Yan, D. I. Schuster, and A. N. Cleland, Deterministic multi-qubit entanglement in a quantum network, *Nature* **590**, 571 (2021).
- [22] A. Gold, J. Paquette, A. Stockklauser, M. J. Reagor, M. S. Alam, A. Bestwick, N. Didier, A. Nersisyan, F. Oruc, A. Razavi, B. Scharmann, E. A. Sete, B. Sur, D. Venturelli, C. J. Winkleblack, F. Wudarski, M. Harburn, and C. Rigetti, Entanglement across separate silicon dies in a modular superconducting qubit device, [arXiv:2102.13293](https://arxiv.org/abs/2102.13293) [quant-ph] (2021).
- [23] R. H. Koch, J. Clarke, W. M. Goubau, J. M. Martinis, C. M. Pegrum, and D. J. van Harlingen, Flicker ($1/f$) noise in tunnel junction dc SQUIDs, *J. Low Temp. Phys.* **51**, 207 (1983).
- [24] F. C. Wellstood, C. Urbina, and J. Clarke, Low-frequency noise in dc superconducting quantum interference devices below 1 K, *Appl. Phys. Lett.* **50**, 772 (1987).
- [25] D. Vion, A. Aassime, A. Cottet, P. Joyez, H. Pothier, C. Urbina, D. Esteve, and M. H. Devoret, Manipulating the quantum state of an electrical circuit, *Science* **296**, 886 (2002).
- [26] J. M. Martinis, S. Nam, J. Aumentado, K. M. Lang, and C. Urbina, Decoherence of a superconducting qubit due to bias noise, *Phys. Rev. B* **67**, 094510 (2003).
- [27] G. Ithier, E. Collin, P. Joyez, P. J. Meeson, D. Vion, D. Esteve, F. Chiarello, A. Shnirman, Y. Makhlin, J. Schrieffer, and G. Schön, Decoherence in a superconducting quantum bit circuit, *Phys. Rev. B* **72**, 134519 (2005).
- [28] F. Yoshihara, K. Harrabi, A. O. Niskanen, Y. Nakamura, and J. S. Tsai, Decoherence of Flux Qubits due to $1/f$ Flux Noise, *Phys. Rev. Lett.* **97**, 167001 (2006).
- [29] R. C. Bialczak, R. McDermott, M. Ansmann, M. Hofheinz, N. Katz, E. Lucero, M. Neeley, A. D. O'Connell, H. Wang, A. N. Cleland, and J. M. Martinis, $1/f$ Flux Noise in Josephson Phase Qubits, *Phys. Rev. Lett.* **99**, 187006 (2007).
- [30] R. H. Koch, D. P. DiVincenzo, and J. Clarke, Model for $1/f$ Flux Noise in SQUIDs and Qubits, *Phys. Rev. Lett.* **98**, 267003 (2007).
- [31] L. Faoro and L. B. Ioffe, Microscopic Origin of Low-Frequency Flux Noise in Josephson Circuits, *Phys. Rev. Lett.* **100**, 227005 (2008).
- [32] V. E. Manucharyan, J. Koch, L. I. Glazman, and M. H. Devoret, Fluxonium: single Cooper-pair circuit free of charge offsets, *Science* **326**, 113 (2009).
- [33] R. Barends, J. Kelly, A. Megrant, D. Sank, E. Jeffrey, Y. Chen, Y. Yin, B. Chiaro, J. Mutus, C. Neill, P. O'Malley, P. Roushan, J. Wenner, T. C. White, A. N. Cleland, and J. M. Martinis, Coherent Josephson Qubit Suitable for Scalable Quantum Integrated Circuits, *Phys. Rev. Lett.* **111**, 080502 (2013).
- [34] P. J. J. O'Malley *et al.*, Qubit Metrology of Ultralow Phase Noise Using Randomized Benchmarking, *Phys. Rev. Appl.* **3**, 044009 (2015).
- [35] P. Kumar, S. Sendelbach, M. A. Beck, J. W. Freeland, Z. Wang, H. Wang, C. C. Yu, R. Q. Wu, D. P. Pappas, and R. McDermott, Origin and Reduction of $1/f$ Magnetic Flux Noise in Superconducting Devices, *Phys. Rev. Appl.* **6**, 041001(R) (2016).
- [36] F. Yan, S. Gustavsson, A. Kamal, J. Birenbaum, A. P. Sears, D. Hover, T. J. Gudmundsen, D. Rosenberg, G. Samach, S. Weber, J. L. Yoder, T. P. Orlando, J. Clarke, A. J. Kerman, and W. D. Oliver, The flux qubit revisited to enhance coherence and reproducibility, *Nat. Commun.* **7**, 12964 (2016).
- [37] M. D. Hutchings, J. B. Hertzberg, Y. Liu, N. T. Bronn, G. A. Keefe, M. Brink, J. M. Chow, and B. L. T. Plourde, Tunable Superconducting Qubits with Flux-Independent Coherence, *Phys. Rev. Appl.* **8**, 044003 (2017).
- [38] A. Kou, W. C. Smith, U. Vool, R. T. Brierley, H. Meier, L. Frunzio, S. M. Girvin, L. I. Glazman, and M. H. Devoret, Fluxonium-Based Artificial Molecule with a Tunable Magnetic Moment, *Phys. Rev. X* **7**, 031037 (2017).

- [39] C. M. Quintana *et al.*, Observation of Classical-Quantum Crossover of $1/f$ Flux Noise and its Paramagnetic Temperature Dependence, *Phys. Rev. Lett.* **118**, 057702 (2017).
- [40] X. You, J. A. Sauls, and J. Koch, Circuit quantization in the presence of time-dependent external flux, *Phys. Rev. B* **99**, 174512 (2019).
- [41] M. A. Rol, F. Battistel, F. K. Malinowski, C. C. Bultink, B. M. Tarasinski, R. Vollmer, N. Haider, N. Muthusubramanian, A. Bruno, B. M. Terhal, and L. DiCarlo, Fast, High-Fidelity Conditional-Phase Gate Exploiting Leakage Interference in Weakly Anharmonic Superconducting Qubits, *Phys. Rev. Lett.* **123**, 120502 (2019).
- [42] Z. Huang, P. S. Mundada, A. Gyenis, D. I. Schuster, A. A. Houck, and J. Koch, Engineering Dynamical Sweet Spots to Protect Qubits from $1/f$ Noise, *Phys. Rev. Appl.* **15**, 034065 (2021).
- [43] P. S. Mundada, A. Gyenis, Z. Huang, J. Koch, and A. A. Houck, Floquet-Engineered Enhancement of Coherence Times in a Driven Fluxonium Qubit, *Phys. Rev. Appl.* **14**, 054033 (2020).
- [44] S. Bertaina, H. Vezin, H. D. Raedt, and I. Chiorescu, Experimental protection of quantum coherence by using a phase-tunable image drive, *Sci. Rep.* **10**, 21643 (2020).
- [45] K. C. Miao, J. P. Blanton, C. P. Anderson, A. Bourassa, A. L. Crook, G. Wolfowicz, H. Abe, T. Ohshima, and D. D. Awschalom, Universal coherence protection in a solid-state spin qubit, *Science* **369**, 1493 (2020).
- [46] N. Didier, E. A. Sete, J. Combes, and M. P. da Silva, AC Flux Sweet Spots in Parametrically Modulated Superconducting Qubits, *Phys. Rev. Appl.* **12**, 054015 (2019).
- [47] N. Didier, Flux control of superconducting qubits at dynamical sweet spots, [arXiv:1912.09416](https://arxiv.org/abs/1912.09416) [quant-ph] (2019).
- [48] P. Bertet, C. J. P. M. Harmans, and J. E. Mooij, Parametric coupling for superconducting qubits, *Phys. Rev. B* **73**, 064512 (2006).
- [49] A. O. Niskanen, K. Harrabi, F. Yoshihara, Y. Nakamura, S. Lloyd, and J. S. Tsai, Quantum coherent tunable coupling of superconducting qubits, *Science* **316**, 723 (2007).
- [50] C. T. Rigetti, Ph.D. thesis, Yale University, 2009.
- [51] F. Beaudoin, M. P. da Silva, Z. Dutton, and A. Blais, First-order sidebands in circuit qed using qubit frequency modulation, *Phys. Rev. A* **86**, 022305 (2012).
- [52] J. D. Strand, M. Ware, F. Beaudoin, T. A. Ohki, B. R. Johnson, A. Blais, and B. L. T. Plourde, First-order sideband transitions with flux-driven asymmetric transmon qubits, *Phys. Rev. B* **87**, 220505(R) (2013).
- [53] D. C. McKay, S. Filipp, A. Mezzacapo, E. Magesan, J. M. Chow, and J. M. Gambetta, Universal Gate for Fixed-Frequency Qubits via a Tunable Bus, *Phys. Rev. Appl.* **6**, 064007 (2016).
- [54] R. K. Naik, N. Leung, S. Chakram, P. Groszkowski, Y. Lu, N. Earnest, D. C. McKay, J. Koch, and D. I. Schuster, Random access quantum information processors using multimode circuit quantum electrodynamics, *Nat. Commun.* **8**, 1904 (2017).
- [55] M. Roth, M. Ganzhorn, N. Moll, S. Filipp, G. Salis, and S. Schmidt, Analysis of a parametrically driven exchange-type gate and a two-photon excitation gate between superconducting qubits, *Phys. Rev. A* **96**, 062323 (2017).
- [56] P. Mundada, G. Zhang, T. Hazard, and A. Houck, Suppression of Qubit Crosstalk in a Tunable Coupling Superconducting Circuit, *Phys. Rev. Appl.* **12**, 054023 (2019).
- [57] M. Reagor *et al.*, Demonstration of universal parametric entangling gates on a multi-qubit lattice, *Sci. Adv.* **4**, eaao3603 (2018).
- [58] S. A. Caldwell *et al.*, Parametrically Activated Entangling Gates Using Transmon Qubits, *Phys. Rev. Appl.* **10**, 034050 (2018).
- [59] S. S. Hong, A. T. Papageorge, P. Sivarajah, G. Crossman, N. Didier, A. M. Polloreno, E. A. Sete, S. W. Turkowski, M. P. da Silva, and B. R. Johnson, Demonstration of a parametrically activated entangling gate protected from flux noise, *Phys. Rev. A* **101**, 012302 (2020).
- [60] D. M. Abrams, N. Didier, B. R. Johnson, M. P. d. Silva, and C. A. Ryan, Implementation of XY entangling gates with a single calibrated pulse, *Nat. Electron.* **3**, 744 (2020).
- [61] E. S. Fried, P. Sivarajah, N. Didier, E. A. Sete, M. P. da Silva, B. R. Johnson, and C. A. Ryan, Assessing the influence of broadband instrumentation noise on parametrically modulated superconducting qubits, [arXiv:1908.11370](https://arxiv.org/abs/1908.11370) (2019).
- [62] N. Didier, E. A. Sete, M. P. da Silva, and C. Rigetti, Analytical modeling of parametrically modulated transmon qubits, *Phys. Rev. A* **97**, 022330 (2018).
- [63] J. Koch, T. M. Yu, J. Gambetta, A. A. Houck, D. I. Schuster, J. Majer, A. Blais, M. H. Devoret, S. M. Girvin, and R. J. Schoelkopf, Charge-insensitive qubit design derived from the cooper pair box, *Phys. Rev. A* **76**, 042319 (2007).
- [64] P. Krantz, M. Kjaergaard, F. Yan, T. P. Orlando, S. Gustavsson, and W. D. Oliver, A quantum engineer's guide to superconducting qubits, *Appl. Phys. Rev.* **6**, 021318 (2019).
- [65] I. L. Chuang and M. A. Nielsen, Prescription for experimental determination of the dynamics of a quantum black box, *J. Mod. Opt.* **44**, 2455 (1997).
- [66] M. A. Nielsen, A simple formula for the average gate fidelity of a quantum dynamical operation, *Phys. Lett. A* **303**, 249 (2002).
- [67] C. A. Ryan, B. R. Johnson, J. M. Gambetta, J. M. Chow, M. P. da Silva, O. E. Dial, and T. A. Ohki, Tomography via correlation of noisy measurement records, *Phys. Rev. A* **91**, 022118 (2015).
- [68] E. Knill, D. Leibfried, R. Reichle, J. Britton, R. B. Blakestad, J. D. Jost, C. Langer, R. Ozeri, S. Seidelin, and D. J. Wineland, Randomized benchmarking of quantum gates, *Phys. Rev. A* **77**, 012307 (2008).
- [69] E. Magesan, J. M. Gambetta, B. R. Johnson, C. A. Ryan, J. M. Chow, S. T. Merkel, M. P. da Silva, G. A. Keefe, M. B. Rothwell, T. A. Ohki, M. B. Ketchen, and M. Steffen, Efficient Measurement of Quantum Gate Error by Interleaved Randomized Benchmarking, *Phys. Rev. Lett.* **109**, 080505 (2012).
- [70] E. A. Sete, N. Didier, A. Q. Chen, S. Kulshreshtha, R. Manenti, and S. Poletto, Parametric-resonance entangling gates with a tunable coupler, [arXiv:2104.03511](https://arxiv.org/abs/2104.03511) [quant-ph] (2021).
- [71] P. J. Karalekas, N. A. Tezak, E. C. Peterson, C. A. Ryan, M. P. da Silva, and R. S. Smith, A quantum-classical cloud platform optimized for variational hybrid algorithms, *Quantum Sci. Technol.* **5**, 024003 (2020).